

The Causes of Halo Shape Changes Induced by Cooling Baryons: Disks Versus Substructures

Victor P. Debattista^{1,2}, Ben Moore³, Thomas Quinn¹, Stelios Kazantzidis⁴, Ryan Maas¹,
Lucio Mayer³, Justin Read³, Joachim Stadel³

ABSTRACT

Cold dark matter cosmogony predicts triaxial dark matter halos, whereas observations find quite round halos. This is most likely due to the condensation of baryons leading to rounder halos. We examine the halo phase space distribution basis for such shape changes. Triaxial halos are supported by box orbits, which pass arbitrarily close to the density center. The decrease in triaxiality caused by baryons is thought to be due to the scattering of these orbits. We test this hypothesis with simulations of disks grown inside triaxial halos. After the disks are grown we check whether the phase space structure has changed by evaporating the disks and comparing the initial and final states. While the halos are substantially rounder when the disk is at full mass, their final shape after the disk is evaporated is not much different from the initial. Likewise, the halo becomes (more) radially anisotropic when the disk is grown, but the final anisotropy is consistent with the initial. Only if the baryons are unreasonably compact or massive does the halo change irreversibly. We show that the character of individual orbits is not generally changed by the growing mass. Thus the central condensation of baryons does not destroy enough box orbits to cause the shape change. Rather, box orbits merely become rounder along with the global potential. However, if angular momentum is transferred to the halo, either via satellites or via bars, a large irreversible change in the halo distribution

¹Astronomy Department, University of Washington, Box 351580, Seattle, WA 98195, debattis;trq;maas@astro.washington.edu.

²Brooks Prize Fellow

³Department of Theoretical Physics, University of Zürich, Winterthurerstrasse 190, CH-8057, Zürich, Switzerland moore;lucio;justin;stadel@physik.unizh.ch.

⁴Kavli Institute for Particle Astrophysics and Cosmology, Department of Physics, Stanford University, P.O. Box 20450, MS 29, Stanford, CA 94309; stelios@slac.stanford.edu.

occurs. The ability of satellites to alter the phase space distribution of the halo is of particular concern to galaxy formation simulations since halo triaxiality can profoundly influence the evolution of disks.

Subject headings: galaxies: evolution — galaxies: formation — galaxies: halos — dark matter

1. Introduction

The dark matter halos that form via hierarchical growth in the cold dark matter (CDM) cosmologies are generally triaxial with mean axial ratios $b/a \sim 0.6$ and $c/a \sim 0.4$, where $c < b < a$ are the short, intermediate, and long axes, respectively (Bardeen et al. 1986; Barnes & Efstathiou 1987; Frenk et al. 1988; Dubinski & Carlberg 1991; Jing & Suto 2002; Bailin & Steinmetz 2005; Allgood et al. 2006). Observational constraints on halo shapes can be obtained from the Milky Way (Ibata et al. 2001; Johnston et al. 2005; Helmi 2004; Fellhauer et al. 2006), from polar ring galaxies (Schweizer et al. 1983; Sackett & Sparke 1990; Iodice et al. 2003), from X-ray isophotal shapes (Buote & Canizares 1994; Buote et al. 2002) (but see also Diehl & Statler 2007), and from gravitational lensing (Kochanek 1995; Bartelmann et al. 1995; Koopmans et al. 1998; Oguri et al. 2003). For disk galaxies, or disks surrounding elliptical galaxies, the ellipticity of the potential in the mid-plane, ϵ_{Φ} , can be constrained through photometry and/or kinematics of stars or gas (e.g., Franx & de Zeeuw 1992; Huizinga & van Albada 1992; Kuijken & Tremaine 1994; Franx et al. 1994; Schoenmakers et al. 1997; Andersen et al. 2001; Debattista 2003; Barnes & Sellwood 2003; ?). The general consensus from these studies is that dark matter halos are rounder than those predicted by collisionless CDM simulations. But this need not be in disagreement with CDM since the condensation of baryons to the centers of halos has been shown to lead to rounder halos (Dubinski 1994; Kazantzidis et al. 2004). For example, Kazantzidis et al. (2004) find that the principal axis ratios increase by $\sim 0.2 - 0.4$ in the inner regions (although triaxiality is not completely erased) extending to almost the virial radius.

Slowly rotating triaxial structures can be supported by centrophilic box orbits (Schwarzschild 1979; Gerhard & Binney 1985; Statler 1987; Udry & Martinet 1994; Fridman & Merritt 1997; Valluri & Merritt 1998). Several studies have shown that when a black hole is present scattering of box orbits is responsible for causing an elliptical galaxy to become rounder, or at least axisymmetric (Lake & Norman 1983; Gerhard & Binney 1985; Norman et al. 1985; Merritt & Quinlan 1998; Valluri & Merritt 1998; Holley-Bockelmann et al. 2002; Kalapotharakos et al. 2004). These scattering events lead to a large number of orbits becoming chaotic. Chaos by itself, however, need not be a fundamental limit to forming long-lived triaxial struc-

tures: using orbit superposition, Poon & Merritt (2002) were able to construct long-lived triaxial models of nuclei even in the presence of a large fraction ($\gtrsim 50\%$) of chaotic orbits. If axisymmetrization does occur, Gerhard & Binney (1985) predict that it is largely confined to the center and occurs gradually. The N -body simulations of a cored system by Merritt & Quinlan (1998) instead found that the axisymmetrization extends to the entire system and occurs on a crossing time for black holes of mass $\sim 2\%$ of the galaxy’s mass. When instead the system is cuspy, Holley-Bockelmann et al. (2002) found that black holes do not lead to a global axisymmetrization of the system. Triaxial structures in disks (*i.e.* bars) can also be destroyed by central mass concentrations (CMCs). The main mechanism is again scattering by the CMC. Although the main bar-supporting orbit family, the x_1 orbits (Contopoulos 1980), is a centrophobic loop family, stars librating about the closed x_1 orbits can still get close to the center and then be scattered by a CMC. Simulations have shown that the required mass for a soft CMC (*i.e.* one with a scale of a few 100 pc) is an unrealistically large $\sim 20\%$ of the disk mass, while the mass required of a hard CMC (few parsecs or less scale) is $\sim 5\%$ of the disk mass (Shen & Sellwood 2004; Athanassoula et al. 2005; Debattista et al. 2006), which is much larger than typical supermassive black holes.

Likewise, it has often been assumed that the loss of halo triaxiality when baryons cool inside halos is partly or mostly due to the destruction of box orbits, which pass arbitrarily close to the center after a sufficiently long time. The fate of box orbits in the presence of disks is of interest for various reasons beside the shape of the halo. Box orbits play an important role in speeding up the mergers of supermassive black holes at the centers of galaxies (Merritt & Poon 2004). Moreover, box orbits lead to radial anisotropy, whereas the destruction of box orbits results in tangential anisotropy. This in turn affects the event rate and energies of dark matter detection experiments involving both direct scattering and indirect annihilation from capture by the Sun or the Earth (see the review by Jungman et al. 1996).

In order to help shed light on these issues, we test whether box orbit scattering is responsible for triaxial halos becoming rounder when baryons cool inside them. We do this via simulations in which we first grow and then evaporate disks inside triaxial halos. Such evaporation, while obviously unphysical, allows us to directly assess the impact of disks on halos by comparing the initial and final states. After the disks are grown, we find that the halos become substantially rounder and their kinematics radially anisotropic. But comparing their initial and final shapes when the disk mass is zero in both cases, we find that the changes are largely reversible. The destruction of box orbits being irreversible, halos should not recover their initial states if this is the main cause of the shape change. We also show that if angular momentum is transferred to the halo (via bars or satellites), then the irreversible changes are substantially larger.

Section 2 of this paper discusses the N -body methods used in this study. Section 3 presents the results of simulations with growing rigid central massive objects. In §4 we present simulations in which angular momentum is transferred to the halo either by a live bar or by satellites. Section 5 presents a preliminary analysis of the orbital evolution for a subsample of the simulations. Our conclusions are presented in §6.

2. Numerical Methods

The basis of this work is that box orbit destruction is an irreversible process. Rather than following all orbits, we adiabatically grow and then evaporate a disk to show that the distribution function of a halo is not substantially changed despite the fact that the halo appears very different when the disk is at full mass. Of course, evaporating the disk is a purely numerical contrivance, but this allows us to test for halo distribution function changes directly. Although classical mechanics are time-reversible, the random phases of any scattered orbits ensure that simply evaporating the central mass is not enough to return to the initial configuration. This would only be possible if we had a perfect integrator and if we had reversed all velocities, which we did not do.

We formed prolate/triaxial halos via mergers, as described in Moore et al. (2004). The initial spherical halos were generated from a distribution function using the method described in Kazantzidis et al. (2004) with the added refinement that each halo is composed of two mass species arranged on shells. The outer shell has more massive particles than the inner one, in order to increase the effective resolution in the central parts. Our model halo A was generated by the head-on merger of two prolate halos, themselves the product of a binary merger of spherical systems. The first merger placed the concentration $c = 10$ halos 800 kpc apart approaching each other at 50 km s^{-1} , while the second merger starts with the remnant at rest, 400 kpc from an identical copy. The resulting halo is highly prolate with a mild triaxiality. Halo model B was produced by the merger of two spherical halos starting at rest, 800 kpc apart. Both halos A and B consist of 4×10^6 particles. The outer particles are ~ 18 times more massive in halo A and ~ 5 times more massive in halo B. A large part of the segregation by particle mass persists after the mergers and the small radius regions are dominated by low mass particles (cf. Dehnen 2005). Figure 1 shows the particle segregation in the case of halo A. We used a softening parameter $\epsilon = 0.1 \text{ kpc}$ for all halo particles, although we have verified that using a larger softening, $\epsilon = 1 \text{ kpc}$, for the more massive species does not change our results. Our force resolution was chosen to be smaller than the vertical scale of the disk, thereby resolving short-range forces.

Once we produced the prolate/triaxial halos, we inserted a disk of particles that remains

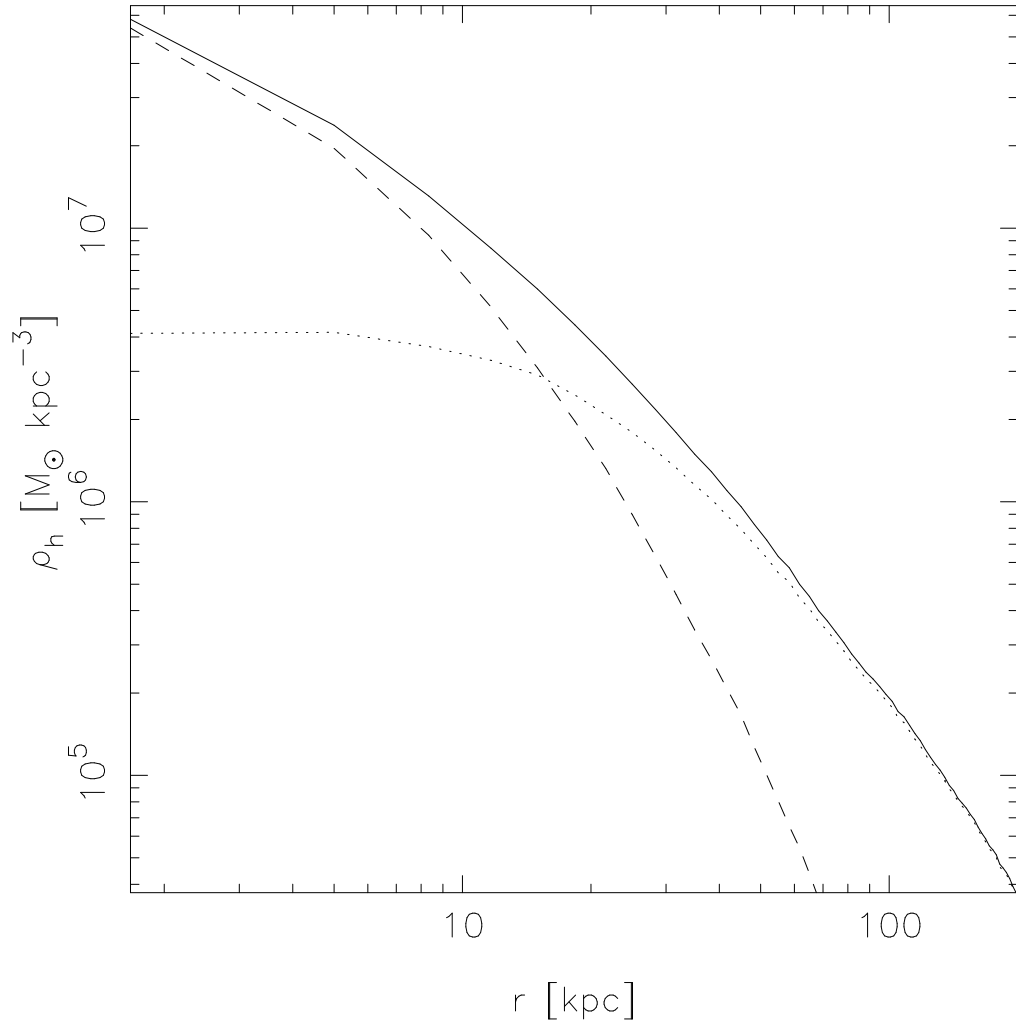


Fig. 1.— Spherically averaged density profile of dark matter particles in halo A before any baryons are introduced. The solid line is the full density profile, the dashed line is for the lower mass species, while the dotted line is for the higher mass species.

rigid throughout the experiments. In all mergers we have been careful to either give the halo no angular momentum, or to place the disk’s symmetry axis along the angular momentum of the halo since otherwise additional evolution would result (Debattista & Sellwood 1999). The disks are composed of $300K$ equal-mass particles each with a softening $\epsilon = 60 - 100$ pc. The disk distribution was, in all cases, exponential with scale length R_d and Gaussian scale-height $z_d/R_d = 0.05$. The disks were placed at various orientations within the halos. We refer to these experiments by the halo axis along which the disk’s symmetry axis is aligned: in “short-axis” (S) experiments, the symmetry axis of the disk is parallel to the short axis of the halo, while in “long-axis” (L) experiments, the symmetry axis of the disk is along the halo’s major axis. If the halo is triaxial, then an “intermediate-axis” (I) experiment has the disk minor axis parallel to the halo’s intermediate axis. Initially, the disk has negligible mass, but this grows adiabatically linearly over time to a mass M_b during a time t_g . After this time, we slowly evaporated it during a time t_e . Thus,

$$M_{disk}(t) = \begin{cases} M_b \frac{t}{t_g} & 0 \leq t \leq t_g \\ M_b \left(1 - \frac{t-t_g}{t_e}\right) & t_g \leq t \leq t_g + t_e. \end{cases} \quad (1)$$

From $t = 0$ to $t_g + t_e$ the halo particles are free to move and achieve equilibrium with the disk as its mass changes, but all disk particles are frozen in place. Since a triaxial global potential leads to elliptical disks forming, we include one simulation with an elliptical disk.

Another key assumption in these simulations is that the disks form without much transfer of angular momentum to the halo. While formation of realistic galaxies requires that baryons conserve most of their angular momentum (e.g., Sommer-Larsen et al. 1999), gas condensation onto subhalos results in angular momentum transfer to the halo (Navarro & Steinmetz 1997). We therefore present experiments in which a few softened particles were introduced, with a mass grown in the same way. We refer to these experiments by the label “P” subscripted by “f” for particles frozen in place and by “l” for live particles free to move. Lastly, we present one simulation, BA1, in which the disk at t_g is replaced by live particles and evolved for 10 Gyr before evaporating the disk. We set initial disk particle velocities for a constant Toomre- $Q = 1.5$. In setting up the disk kinematics we azimuthally averaged radial and vertical forces. Thus, our disk is initially not in perfect equilibrium, but was close enough that it quickly settled to a new equilibrium.

All the simulations in this paper, which are listed in Table 1, were evolved with PKDGRAV (Stadel 2001), an efficient, multi-stepping, parallel treecode.

Run	Halo	r_{200} [kpc]	M_{200} [$10^{12} M_{\odot}$]	M_b [$10^{11} M_{\odot}$]	R_d [kpc]	t_g [Gyr]	t_e [Gyr]
SA1	A	215	4.5	1.75	3.0	5	2.5
SA2	A	215	4.5	5.25	3.0	5	2.5
SA3	A	215	4.5	1.75	1.5	5	2.5
IA1	A	215	4.5	1.75	3.0	5	2.5
LA1	A	215	4.5	1.75	3.0	5	2.5
LB1	B	106	0.65	1.05	3.0	15	7.0
TA1	A	215	4.5	1.75	3.0	5	2.5
EA1	A	215	4.5	1.75	3.0	5	2.5
BA1	A	215	4.5	0.52	3.0	1.5	2.5
P _l A1	A	215	4.5	1.75	0.5	5	2.5
P _l A2	A	215	4.5	1.75	5.0	5	2.5
P _l B1	B	106	0.65	0.7	3.0	10	4
P _f B2	B	106	0.65	0.7	3.0	10	4
P _l B3	B	106	0.65	0.35	0.1	5	5

Table 1: The simulations in this paper. For the particle simulations (P_lA1-P_lB3), R_d refers to the softening of the particle(s). For runs P_lA1 and P_lA2, the value of M_b refers to the combined mass of all the satellite particles at t_g . The disk in run TA1 is tilted by 30° relative to the one in SA1 whereas the disk in EA1 is elliptical. In run BA1, the disk at t_g was replaced by live particles and evolved for 10 Gyr (during which time a bar formed and then was destroyed), before being evaporated.

2.1. Measuring halo shapes

To measure the axis ratios c/a and b/a we adopt a method based on Katz (1991) that uses the eigenvalues of the (unweighted) moment of inertia tensor I . For each bin of N particles we computed I_{ij} as follows:

$$I_{ij} = \frac{\sum_{k=1}^N m_k r_{i,k} r_{j,k}}{\sum_{k=1}^N m_k}. \quad (2)$$

We then diagonalize I and calculate

$$b/a = \sqrt{\mathcal{I}_{22}/\mathcal{I}_{11}} \quad \text{and} \quad c/a = \sqrt{\mathcal{I}_{33}/\mathcal{I}_{11}}, \quad (3)$$

where the \mathcal{I}_{ii} 's are the eigenvalues of I and $\mathcal{I}_{11} \geq \mathcal{I}_{22} \geq \mathcal{I}_{33}$. A useful parameter for expressing shape is the triaxiality parameter $T = (a^2 - b^2)/(a^2 - c^2)$ (Franx et al. 1991). The cases $T = 0$ and $T = 1$ correspond to oblate and prolate shapes, respectively, while $T = 0.5$ is the maximally triaxial case.

We measured shapes in shells of fixed semi-major axis widths around the center of the system. Thus, these shape measurements are differential, rather than integrated (*cf.* Katz 1991). We use the iterative procedure of Katz (1991) in which the convergence criterion is a variation in axis ratios by $< 0.01\%$. In each iteration the semi major axis of the shell is held fixed; a particle is included in the calculation of I_{ij} if $q_{lo} < q < q_{hi}$, where q is the ellipsoidal radius defined as

$$q^2 = x^2 + \left(\frac{y}{b/a}\right)^2 + \left(\frac{z}{c/a}\right)^2. \quad (4)$$

We used shell widths $q_{hi} - q_{lo} = 5$ kpc for all models.

The center of the system is taken to be the center of mass of a sphere of radius 1 kpc centered on the minimum of the potential and is fixed for all shells. Tests performed in which the center of mass was allowed to vary by up to 0.5 kpc show less than 5% variation in the axis ratios past 10 kpc. Tests in which the limits of each shell were reduced by half around the average radius of that shell gave axis ratios that varied from the full resolution results by up to 0.08 in the worst cases and by less than 0.05 for most runs. Shells were not prevented from overlapping; as a result, some particles are sampled in more than one shell. We have verified that this does not bias our shape estimates through the experiments with the halved shell widths, where the shells never intersect. When the number of particles in the central shell is less than $10K$, then convergence is not reached after 20 iterations, or the axis ratios varies by as much as 20%, so we take this number to be a reasonable cutoff for the reliability of these innermost shells and ignore shells with less particles. This occurs in only two cases, and in general most inner shells have $> 25K$ particles, which we find to be more than enough to ensure consistent measurements with our method.

3. Central Massive Objects

3.1. Short- and Intermediate-Axis Experiments

In run SA1 we grew a disk inside halo A with the minor axes of the disk and halo aligned. This orientation is a natural one for disks to form in since simulations have shown that the angular momenta of halos are aligned with their *minor* axes (*e.g.* Warren et al. 1992; Porciani et al. 2002; Faltenbacher et al. 2005). Once the disk is grown to its full mass it dominates the inner rotation curve (see Fig 2, left). The shape evolution of this highly prolate, mildly triaxial halo is shown in Figure 3a. The effect of the massive disk on the halo shape is large: having started out with $b/a \lesssim 0.45$ it becomes much rounder in the plane of the disk ($b/a \gtrsim 0.6$ to 40 kpc, *i.e.* $\sim 0.2 r_{200}$, the disk constituting 17% of the mass within this radius), as shown by the blue lines. The change in shape perpendicular to

the disk is more modest and the inner halo becomes significantly more triaxial than when it started out. In the disk plane, the combined potential starts out very elliptical, $\epsilon_\Phi \simeq 0.4$, and becomes quite round, with $\epsilon_\Phi < 0.1$ over the entire extent of the disk (Fig. 4). This ϵ_Φ is sufficiently small to be consistent with the observed scatter in the Tully-Fisher relation (Franx & de Zeeuw 1992), even without the additional axisymmetrization of the potential that would be caused by the disk’s orthogonal response. Once the disk is evaporated, the resulting halo shape, shown by the green lines in Figure 3a, is very similar to its original shape, with the net increase in both b/a and c/a being $\lesssim 0.1$ throughout the inner 100 kpc. The final triaxiality is barely changed from the starting one, despite the fact that the inner halo was almost maximally triaxial at t_g .

Likewise, the final density and anisotropy profiles, shown in Figure 5, are not significantly changed, despite the factor of ~ 3.7 increase in halo central density at t_g . The halo anisotropy, $\beta = 1 - \sigma_t^2/\sigma_r^2$, where $\sigma_t^2 = \frac{1}{2}(\sigma_\theta^2 + \sigma_\phi^2)$, starts out $\beta \simeq 0$, grows to $\beta \gtrsim 0.2$ at t_g (*i.e.* becomes radially anisotropic), and returns to $\beta \simeq 0$ at $t_g + t_e$. If box orbits had been destroyed to any significant extent, we would have seen instead an increase in tangential anisotropy (e.g., Holley-Bockelmann et al. 2002).

The small difference between $t = 0$ and $t_g + t_e$ in halo shape and kinematics suggests that the halo phase space distribution has not been grossly altered by the presence of the massive disk. There is little evidence for a substantial amount of box orbit scattering, and any chaos induced has to be quite mild. All this is true despite the quite large change in halo shape and kinematics when the disk is at full mass.

Figure 3a (*yellow and red lines*) also shows the evolution when we left the disk at full mass for 5 Gyr before evaporating it. The halo becomes slightly rounder (by about $b/a \lesssim 0.1$) at all radii both after the additional 5 Gyr and once the disk is evaporated. The difference is largest inside ~ 30 kpc where the final b/a and c/a are about 0.1 larger at the end of the simulation. This difference must be due to orbit scattering (either physical or purely numerical); the fact that the difference between these two runs is so much smaller than that between $t = 0$ and t_g implies that scattering has only a mild effect on the halo shape. The global shape change at t_g can therefore be attributed to orbit deformation.

Model SA1 had a disk with $R_d = 3$ kpc and a baryon-to-dark matter fraction, $f_b = 0.039$, consistent with estimates for local galaxies (Jimenez et al. 2003). A more massive or more compact galaxy may lead to greater scattering. We explored to what extent larger f_b or smaller R_d affect the halo shape in two further simulations. Run SA2 increased M_b by a factor of 3 while keeping R_d fixed. The halo shape is changed significantly all the way out to r_{200} once the disk is evaporated, but remains quite prolate, with $b/a < 0.6$ and $c/a < 0.5$, as can be seen in Figure 3b. In contrast, at t_g the halo has $0.5 < b/a < 1.0$ within the

inner 50 kpc. Even with this high $f_b \simeq 0.12$, or $\sim 70\%$ of the full cosmic baryon fraction (Spergel & et al. 2006), the irreversible change to the halo shape is $\lesssim 50\%$ of the full change at t_g out to 100 kpc. Run SA3 instead set $R_d = 1.5$ kpc, keeping the ratio z_d/R_d fixed (and decreasing all softenings appropriately). The evolution in this case is shown in Figure 3c; as in run SA1, although the halo at $t = t_g$ is substantially rounder than at the start, after the disk is evaporated the halo recovers most of its original shape. Of runs SA2 and SA3, making the disk more massive (SA2) produced a larger irreversible change in the halo than did making it more compact.

Run IA1 explored whether having the disk orthogonal to the intermediate axis makes a significant difference to the halo distribution, with all other parameters as in run SA1. The resulting shape evolution is presented in Figure 3d. In this simulation the halo at t_g remained more elongated than that in run SA1 despite having the same M_b . The axis ratios of the halo at t_g cross over at ~ 30 kpc, where the halo’s flattening orthogonal to the disk causes the minor axis to switch from the disk plane to the orthogonal direction. Once the disk is evaporated, the halo ends very nearly axisymmetric in cross section in this inner region but continues to be highly prolate. As in run SA1, the net change in halo shape is relatively small at $t_g + t_e$.

3.2. Long-Axis Experiments

In run LA1 we placed the disk with its symmetry axis along the long axis of the halo. This orientation has been suggested to be favored by the distribution of satellites around the Milky Way (Zentner et al. 2005) and by the Sagittarius dwarf tidal stream (Helmi (2004) but see Fellhauer et al. (2006) for a different view). Other than the disk’s orientation, the parameters of this model are identical to those of run SA1. As in that model, the halo in run LA1 is significantly deformed to large radius by the growing disk, but it recovers its shape nearly completely once the disk is evaporated, as shown in Figure 3e. Likewise, the spherically averaged kinematic evolution of run LA1 is indistinguishable from that of SA1, as seen in Figure 5.

A unique characteristic of the evolution in long-axis experiments is their tendency for the major axis of the inner halo to switch orientation by 90° into the disk plane once the disk grows sufficiently massive. For run LA1 this is evident in Figure 3e, which shows that the halo is axisymmetric at ~ 20 kpc (the solid blue line approaches $b/a \simeq 1$, while the dot-dashed blue line approaches $T \simeq 0$) but is quite prolate-triaxial at smaller radii. Major axis flips are more clearly illustrated by the nearly axisymmetric halo B. In run LB1, as M_{disk} increases, shells of the prolate inner halo become spherically symmetric. Further increase in

M_{disk} then leads to the shell becoming not only flatter vertically (relative to the disk) but also acquiring an *elongation* with its major axis in the plane of the disk, *i.e.* the symmetry axis of the inner halo flips by 90° and becomes orthogonal to that of the outer halo (see Figs. 6 and 7). The direction along which this reorientation occurs is not random since the halo is initially not perfectly axisymmetric on large scales. Continued increase in M_{disk} causes the symmetry axis to flip orientation to larger radii, eventually saturating at ~ 10 kpc. The halo orientation flips do not occur when the disk is replaced by a point particle. The dotted gray line in Figure 7 shows the orientation of the major axis in run P_lB1, at a time when its mass is the same as that in LB1; no flip in the major axis direction can be seen.

3.3. Inclined Disk

Simulations have found that the angular momenta of the halo and gas need not be aligned (van den Bosch et al. 2002; Chen et al. 2003), although the inner halo and the disk that would form settle to a common plane (Dubinski & Kuijken 1995). Therefore we also explored the effect of a disk inclined relative to the main plane of the dark matter halo. Run TA1 is based on run SA1 but with the disk inclined by 30° about the y -axis (intermediate axis), all other parameters being the same. The resulting evolution is virtually indistinguishable from that in run SA1 at all times, as shown in Figure 8a.

3.4. Elliptical Disk

A disk forming in an elliptical potential becomes elongated with its major axis orthogonal to that of the potential (e.g., Gerhard & Vietri 1986). In run EA1 we replaced the disk in run SA1 by an elliptical disk, with its long axis along the y -axis. We obtain this oval disk by shrinking the x coordinates (parallel to the halo major axis) of all disk particles by a factor of 0.75; *i.e.*, the ellipticity of the disk density was $\epsilon = 1 - b/a = 0.25$. The degree to which elliptical disks change halo distributions is over estimated by this simulation since the disk ellipticity is quite large for a massive disk. We then evolved this system identically to run SA1, keeping the disk fixed in place. Figure 8b compares the shape evolution with that in run SA1. At $t_g + t_e$ the halo is left significantly rounder within ~ 20 kpc than it was in run SA1, but beyond that the evolution is very similar.

3.5. Central Softened Point Masses

All of the experiments described above had rigid disks frozen in place. While we have been careful to recenter the halo in position and velocity after the mergers and before growing the disks, some residual relative motion of the inner and outer parts of the halos remained. This motion is damped as the mass of the disk increases, possibly causing some scattering of orbits. In order to test for artifacts associated with such damping, we resorted to simulations with only a single baryonic particle and compared the evolution when the particle is free to move (P_lB1) and when it is frozen in place (P_fB2). The rotation curve at t_g is shown in Figure 2. Figure 3g shows their shape evolution; in both cases, the shape is largely recovered at $t_g + t_e$. If anything, P_lB1 is very slightly rounder at 10 kpc than P_fB2 compared with the initial halo. Figure 5 shows that their density and kinematic evolution also is largely reversible. Thus, our use of rigid disks nailed in place could not have induced much artificial orbit scattering.

3.6. Ultrahard particle

In runs P_lB1 and P_fB2 the growing particle had a softening of $\epsilon = 3$ kpc, a reasonable size for a galaxy. In run P_lB3 we decreased the softening length of the particle to 100 pc and M_b by half. Despite the smaller M_b the final halo after $t_g + t_e$ remains substantially rounder inside 20 kpc than in those runs (but is largely recovered at larger radii). If the central particle were a black hole, its sphere of influence assuming $\sigma_0 = 100$ km s⁻¹ from $t = 0$ would be ~ 15 kpc. This is comparable to the radius out to which the particle irreversibly alters the shape of the halo. Likewise, the halo mass within 20 kpc is comparable to that of the central particle: at $t = 0$, the halo mass within this radius is $4M_b$. Unlike runs P_lB1 and P_fB2, Figure 5 shows that the kinematic evolution is not reversible, and the halo of run P_lB3 becomes significantly tangentially anisotropic, as expected if box orbits are destroyed. Despite the different final state, Figure 3h also shows that the halo shape at t_g is not much different from that in P_lB1 and P_fB2, implying that halo shape change is not dominated by scattering. Whereas run SA3 with $R_d = 1.5$ kpc, which is not unreasonably small for most galaxies, did not significantly cause box orbit destruction, the ~ 10 times more centrally concentrated run P_lB3 is able to cause a large irreversible change to the halo shape out to $\sim 0.3 r_{200}$. However, $R_d/r_{200} \simeq 0.001$ is unrealistically small.

4. Angular Momentum Transport

We next explore the effect of angular momentum transfer to the halo. Such transfer is irreversible so the change inflicted on the halo must also be irreversible. How strongly the halo distribution is changed depends on the mechanism by which angular momentum is transferred. If via bars or spirals then we may expect that the changes are mostly at small radius. If angular momentum is transferred by satellite galaxies, however, then the effect on the halo is likely to be much more widespread.

4.1. Live Barred Disk

In run BA1 we evolved a model with a live disk for 10 Gyr after t_g before evaporating the disk. The initial system was similar to run SA1 but with only 30% of its M_b . We chose this lower mass because the same mass as SA1 leads to a long-lived bar, whereas we are interested in forming a bar that gets destroyed in order to be able to evaporate the disk. A bar quickly formed and was subsequently destroyed (Berentzen et al. 2006). After 10 Gyr, we fixed the disk particles in place and evaporated the disk. Very little of the inner halo shape is recovered after the disk is evaporated. In the inner ~ 20 kpc the halo remains rounder than at $t = 0$, with both b/a and c/a larger by $\gtrsim 0.1$. The irreversible change in the halo is associated with the transfer of angular momentum from disk to halo (Weinberg 1985; Debattista & Sellwood 1998). Run BA1 produces a comparable change in the inner 20 kpc of the halo as did the 10 times more massive run SA2, but the shape change is much smaller farther out. Since the bar transfers angular momentum to the halo at resonances (Weinberg 1985), and the strongest of these are at smaller radii (most of the angular momentum gained by the halo is within the inner ~ 10 kpc), this accounts for the relatively small radial extent of the halo shape change.

4.2. Satellites

Baryons need not cool directly onto the central disk but onto satellites instead. The presence of large numbers of dark satellites is one of the main predictions of CDM (Moore et al. 1999; Klypin et al. 1999; Ghigna et al. 2000). As they sink, satellites lose angular momentum to the halo; in the process box orbits may be scattered. We explored this evolution with models P_lA1 and P_lA2. Starting with halo A, we selected 10 particles that stay within 200 kpc but otherwise at random, and adiabatically increased each of their masses to give the same total baryonic mass as in run SA1. We grew these satellites to full mass and then

evaporated them. Each satellite had $\epsilon = 0.5$ kpc in P_lA1 and 5 kpc in P_lA2. Since we only used softened point particles as satellites, which cannot be tidally stripped, their effect on the halo is larger than it would be in nature. Of the 10 satellites, only one remained at $r > 50$ kpc, the rest having fallen to $R < 25$ kpc by the end of the simulation. The evolution of the halo shape in these two models is presented in Figure 3f. After the particles reach their full mass, the halo of run P_lA1 is about as round as that in run SA1. However, the halo does not recover much of its original shape after the particles are evaporated. Clearly, the distribution function of the halo has been altered to a large extent. Figure 5 shows that angular momentum transferred by baryons to the halo can erase the cusp, in agreement with previous results (Tonini et al. 2006; Mashchenko et al. 2006; Read et al. 2006; Weinberg & Katz 2007) although the contraction caused by the growing central mass masks the core. The halo shape change at $t_g + t_e$ is very similar in the two runs because of quite similar angular momentum absorbed by the halo. Because of the difference in softenings, the different baryonic potential at the halo center at t_g accounts for the $b/a \sim 0.1$ difference in shape, with the softer potential supporting the more elongated shape.

5. Orbital Evolution

We explored directly the evolution of the orbital character of the models by considering a subsample of 1000 particles in run SA1 and following their orbits at various points in the simulation. The 1000 particles were randomly chosen from the $t = 0$ distribution such that they were inside $r = 200$ kpc. We then integrated their motion as test particles while holding all the other particles fixed in place. We used a fixed timestep of 0.1 Myr and integrated for 15 Gyr, storing the phase space coordinates of each test particle every 1 Myr. For the same 1000 particles, we carried out this operation at $t = 0$, t_g , and $t_g + t_e$. Because we froze the background potential, in effect we have computed the orbital character of the particles at these three times. The fact that we integrated for 15 Gyr ensures that we have sufficient points on each orbit to properly characterize it. In this paper we demonstrate with a few examples that a large fraction of box-like orbits at $t = 0$ return to very similar box-like orbits at $t_g + t_e$, showing that deformation, not transformation, is responsible for shape change in most cases. We do this by presenting their configuration space projection at each of the three different times. Such an analysis cannot distinguish between box orbits and mildly chaotic, elongated orbits but this is unimportant anyway for our present purposes since we have integrated for over a Hubble time. If they are mildly chaotic, they can still support a triaxial halo. A full analysis of the orbital structure using more sophisticated techniques will be presented elsewhere.

Of the 1000 orbits, we start by presenting nine particles, initially on boxlike orbits, defined such that, at $t = 0$, they (1) remain inside 25 kpc, (2) do not have a fixed sense of rotation relative to any of the three major axes, (3) reach a radius of at least 10 kpc, and (4) get within 0.2 kpc of the center. The evolution of many of the other 991 orbits is qualitatively similar to that of the nine presented here. Figure 9 projects these orbits onto the halo symmetry planes, where the x -axis is the halo’s major axis and the z -axis is the disk’s symmetry axis. Most orbits at $t_g + t_e$ are quite similar to what they looked like at $t = 0$. None of the orbits seem strongly chaotic, neither at t_g nor at $t_g + t_e$, although they may be weakly chaotic. Moreover, most orbits retain a box-like shape at t_g , but have a significantly rounder shape than those at $t = 0$. At t_g , three of the initially box-like orbits become round (orbits ”a”, ”f” and ”h”); of these only orbit h changes character completely, becoming a loop orbit. Some of the orbits have a slight banana shape; in the full sample of orbits we found many cases of strongly banana-shaped orbits. These had a tendency to become more planar but are still distinctly elongated at $t_g + t_e$. In a few cases we also found the opposite occurring — slightly banana orbits becoming more strongly curved — but this was less common. Of the box-like orbits in Figure 9 some are rounder in the (x, y) plane at $t_g + t_e$ (*e.g.*, orbits a, f and i), but some are rounder at $t = 0$ (*e.g.*, orbits c and e), suggesting that differences in shape are due to scattering. What little difference in orbit shape occurs between $t = 0$ and $t_g + t_e$ can probably be attributed to numerical noise. Most importantly, while there is a clear orbit shape deformation at t_g , little orbital transformation has occurred.

We quantify the orbital deformation of the sample of 1000 particles by plotting in Figure 10 σ_y/σ_x , where $\sigma_x^2 = \sum_t x_t^2$ and similarly for σ_y^2 and the sum is over timesteps. The significantly rounder shape of orbits at t_g than $t = 0$ is apparent, with the vast majority of orbits initially aligned with the halo having σ_y/σ_x closer to unity at the later time. Orbits initially elongated along the halo’s minor axis, as well as orbits initially rounder than $\sigma_y/\sigma_x \gtrsim 0.6$ end up round, with $\sigma_y/\sigma_x \simeq 1$. Instead at $t_g + t_e$ the orbits tend to return to their initial elongation, especially for the most elongated orbits. The right panel shows the distribution of σ_y/σ_x ; orbits become substantially rounder at t_g but the population as a whole recovers the original distribution to a large extent once the disk is evaporated.

A comparison of orbital evolution in runs P_fB2 and P_lB3 provides an example of orbit transformation. We again selected 1000 orbits from particles within the inner 200 kpc of halo B at $t = 0$. We integrated their orbits as above but we used the smaller timestep $\delta t = 10^4$ years in the case of P_lB3; for P_fB2 we use $t_g/2$ when the central particle has the same mass as at t_g in model P_lB3. Although we are comparing the two models at the same central particle mass, the orbits at time $t_g + t_e$ in model P_fB2 were computed after the central particle was evaporated from a mass twice that reached in P_lB3. As before, we present in Figure 11 nine orbits that at $t = 0$ are box-like. These boxlike orbits in P_lB3 are more often transformed

than those in run P_fB2. In model P_fB2, only one orbit (orbit f) appears to have changed substantially at the end of the simulation, while orbits a and d become fish orbits (although they may have been librating about fish orbits at $t = 0$). Orbit b is largely unchanged and the remaining orbits are all boxlike. In model P_lB3, orbit e is changed about as much as orbit f in P_fB2. However, four of the nine orbits, f-i, are very strongly transformed by $t_g + t_e$ and are no longer able to support a triaxial shape. Figure 12 compares the distribution of all 1000 particles and a depletion of elongated orbits is evident in P_lB3 compared with run P_fB2.

6. Discussion

6.1. Timesteps

We also performed a number of tests of the numerics to verify that our results are robust. The main concern is the timestep used. Shen & Sellwood (2004) found that too large timesteps result in bars being destroyed too easily, because orbits are not followed accurately near the central mass. Our simulations used multi-stepping. With a base timestep Δt , particles move on timesteps $\Delta t/2^n$, where n is the rung level satisfying the condition $\delta t = \Delta t/2^n < \eta(\epsilon/a)^{1/2}$, and ϵ is the particle’s softening, a is its acceleration and η a tolerance parameter. We used $\eta = 0.2$, a conservative value; with a base timestep $\Delta t = 5$ Myr, simulation SA1 at t_g had a range of timesteps down to $5/2^5 = 0.16$ Myr. If instead we set $\eta = 2$ the timestep distribution only reaches to $5/2 = 2.5$ Myr. The effect of these larger timesteps, shown in Figure 13, is manifest at $r \lesssim 20$ kpc, which remains significantly rounder at $t_g + t_e$ than when $\eta = 0.2$. The quite modest net shape change in our simulations implies that the timesteps we used were sufficiently small to correctly follow the evolution near the center.

6.2. Evidence against box orbit destruction

We have demonstrated that the substantial axisymmetrization caused by a disk growing inside a dark matter halo is largely, although not wholly, reversible. If triaxial halos become rounder because of box orbit destruction (*e.g.* Macciò et al. 2007), then these orbits would have to be repopulated in order for the halo to recover its original shape once the disk is evaporated. Apart from being unlikely for such a highly ordered system as a triaxial halo, this interpretation is not supported by our orbital analysis, which shows that box-like orbits are deformed by realistic disks but not transformed by scattering into new orbits. The strongest

evidence that deformation is a more important process than transformation comes from the ability of particles to return, after the disk is evaporated, to nearly the same orbits as they started from. This makes it implausible that the shape change is due to a large increase in strong chaos. Instead we find that realistic axisymmetric disks are not concentrated or massive enough to cause substantial chaos. In a similar vein, Holley-Bockelmann et al. (2002) found that chaos in triaxial ellipticals is induced by the black hole only, not by the stellar cusp surrounding it. This need not mean, however, that chaos is not enhanced by the disk. It could well be that orbits are becoming weakly chaotic but do not diffuse sufficiently on a Hubble timescale to significantly weaken triaxiality. The shape evolution due to baryons cooling onto a central galaxy can therefore be computed from adiabatic invariants.

The primary role of orbit deformation over transformation is also indicated by the much smaller effects of scattering when it is clear that scattering has occurred. In run SA1 scattering occurred when the disk was maintained at full mass for an additional 5 Gyr before being evaporated. This only caused a small additional change in the final halo shape. Furthermore, comparing runs P_lB1 and P_lB3 , we find that the halo shape at t_g is rather similar, despite the fact that in run P_lB3 box orbits are significantly destroyed. The same is true for runs SA1 and P_lA1 . These examples directly illustrate that box orbit destruction is a much smaller factor in halo shape changes than is orbit deformation.

Weak chaos is consistent with the orbital characterization of Macciò et al. (2007) but does not support their claim that the shape change is largely due to enhanced chaos from the central baryonic mass. Another possibility is that in their simulations chaos could have been caused by gas cooling inside subhalos, which we showed leads to a substantial change in the phase space distribution of the halo.

6.3. Implications for galaxy formation simulations

If baryons cool onto substructures within the halo then box orbits are very efficiently destroyed. Since the evolution of disks can be strongly influenced by halo triaxiality (*e.g.* Ideta & Hozumi 2000), any process that artificially reduces triaxiality can lead to biases in the properties of galaxies forming in cosmological simulations. Agertz et al. (2007) demonstrate that the evolution of gas blobs in smoothed particle hydrodynamics (SPH) simulations is different from that found in Eulerian gas codes. They interpreted this difference as being due to the unphysically poor mixing of traditional SPH, which allows blobs to survive longer in SPH. Moreover, satellites in cosmological simulations tend to have denser, more concentrated gas components than their real counterparts, which makes them harder to strip by ram pressure and tides (Mayer et al. 2007) and thus more likely to artificially enhance

halo shape changes. Baryonic cooling inside substructures is strongly suppressed by feedback from supernovae (Dekel & Silk 1986; Governato et al. 2004, 2007). If simulations do not treat feedback properly or have low resolution, then baryons may condense into concentrated substructures biasing the global evolution of simulated galaxies.

6.4. Summary

Our results can be summarized as follows:

1. The adiabatic growth of disks with realistic sizes and masses inside prolate/triaxial halos leads to a large change in the shape of the halo. Axis ratios change by > 0.2 out to roughly $0.5 r_{200}$. The growth of the disk drives the halo kinematics to larger radial anisotropy. The midplane global potential ellipticity is less than 0.1, consistent with the small scatter in the Tully-Fisher relation (Franx & de Zeeuw 1992).
2. Despite these large changes, the underlying phase space distribution is not grossly altered, as we verified by artificially evaporating the disk and recovering, to a large extent, the original halo. The irreversible change in final halo structure is larger for more massive or more centrally concentrated disks, but is still a relatively small fraction of the total shape change when the disk is at full mass. As in the case of black holes at the centers of cuspy elliptical galaxies (Gerhard & Binney 1985; Holley-Bockelmann et al. 2002), the bulk of the irreversible halo shape change occurs in the inner region of the galaxy. This small irreversible shape change is driven by orbit scattering.
3. Box orbit destruction cannot be the right interpretation for the shape change caused by disk growth. Such a process is not reversible but we found that a large fraction of particles on box-like orbits individually return to very similar orbits after the disk is evaporated. At most only mild chaos is induced. Instead we find that box orbits become deformed by the growing disk, but retain their character, and this seems sufficient to explain the change in shape. In the absence of angular momentum transport or extreme mass/concentration galaxies, very little of the quite large shape change that dark matter halos undergo as baryons condense inside them is due to box orbit destruction. As a result, shape change can be well approximated by adiabatic invariants.
4. Very concentrated structures do lead to scattering and to large irreversible changes in halo shape and kinematics; we found that scales of ~ 100 pc are needed to accomplish this. The irreversible shape change was then restricted to the sphere of influence of this pointlike mass: $r \sim GM/\sigma^2$. Massive disks are also able to change the halo

structure irreversibly, but the mass required, $\sim 70\%$ of the cosmic baryon fraction, is quite high. Even in such cases of scattering, the halo shape with the baryons at full mass is not much different from similar simulations with little scattering, suggesting that it is orbital deformation in the first place that changes the shape of the halo.

5. If baryons transport angular momentum to the halo, a large irreversible change in halo shape and kinematics occurs. Such transfers can occur either because of gas condensing in satellites or nonaxisymmetric structures forming in the disk. Even quite low mass disks are able to alter the inner halo distribution if they can transport angular momentum to the halo. The effect of satellites can be artificially large in simulations of galaxy formation because of the poor mixing in SPH (Agertz et al. 2007) and the too highly concentrated satellites that form (Mayer et al. 2007).
6. When the disk minor axis and halo major axis are aligned, growth of the disk leads to an elongation within the plane of the disk, even when the initial halo is very nearly axisymmetric.

This paper is based in part on work supported by the National Science Foundation under the following NSF programs: Partnerships for Advanced Computational Infrastructure, Distributed Terascale Facility (DTF), and Terascale Extensions: Enhancements to the Extensible Terascale Facility. Many additional simulations were carried out at the University of Zürich on zBox and at the Arctic Region Supercomputing Center. V. P. D. thanks the University of Zürich for hospitality during part of this project. V. P. D. is supported by a Brooks Prize Fellowship in Astrophysics at the University of Washington and receives partial support from NSF ITR grant PHY-0205413. S. K. acknowledges support by the US Department of Energy through a KIPAC Fellowship at Stanford University and the Stanford Linear Accelerator Center. We thank Andrea Macciò and Ioannis Sideris for fruitful discussions and the anonymous referee for comments that helped to improve this paper. V. P. D. thanks Monica Valluri for discussions that helped improve this paper.

REFERENCES

- Agertz, O., et al. 2007, MNRAS, 380, 963
- Allgood, B., Flores, R. A., Primack, J. R., Kravtsov, A. V., Wechsler, R. H., Faltenbacher, A., & Bullock, J. S. 2006, MNRAS, 367, 1781

- Andersen, D. R., Bershad, M. A., Sparke, L. S., Gallagher, J. S., & Wilcots, E. M. 2001, *ApJ*, 551, L131
- Athanassoula, E., Lambert, J. C., & Dehnen, W. 2005, *MNRAS*, 363, 496
- Bailin, J., & Steinmetz, M. 2005, *ApJ*, 627, 647
- Bardeen, J. M., Bond, J. R., Kaiser, N., & Szalay, A. S. 1986, *ApJ*, 304, 15
- Barnes, E. I., & Sellwood, J. A. 2003, *AJ*, 125, 1164
- Barnes, J., & Efstathiou, G. 1987, *ApJ*, 319, 575
- Bartelmann, M., Steinmetz, M., & Weiss, A. 1995, *A&A*, 297, 1
- Berentzen, I., Shlosman, I., & Jogee, S. 2006, *ApJ*, 637, 582
- Buote, D. A., & Canizares, C. R. 1994, *ApJ*, 427, 86
- Buote, D. A., Jeltema, T. E., Canizares, C. R., & Garmire, G. P. 2002, *ApJ*, 577, 183
- Chen, D. N., Jing, Y. P., & Yoshikaw, K. 2003, *ApJ*, 597, 35
- Contopoulos, G. 1980, *A&A*, 81, 198
- Debattista, V. P. 2003, *MNRAS*, 342, 1194
- Debattista, V. P., Mayer, L., Carollo, C. M., Moore, B., Wadsley, J., & Quinn, T. 2006, *ApJ*, 645, 209
- Debattista, V. P., & Sellwood, J. A. 1998, *ApJ*, 493, L5
- Debattista, V. P., & Sellwood, J. A. 1999, *ApJ*, 513, L107
- Dehnen, W. 2005, *MNRAS*, 360, 892
- Dekel, A., & Silk, J. 1986, *ApJ*, 303, 39
- Diehl, S., & Statler, T. S. 2007, *ApJ*, 668, 150
- Dubinski, J. 1994, *ApJ*, 431, 617
- Dubinski, J., & Carlberg, R. G. 1991, *ApJ*, 378, 496
- Dubinski, J., & Kuijken, K. 1995, *ApJ*, 442, 492

- Faltenbacher, A., Allgood, B., Gottlöber, S., Yepes, G., & Hoffman, Y. 2005, MNRAS, 362, 1099
- Fellhauer, M., et al. 2006, ApJ, 651, 167
- Franx, M., & de Zeeuw, T. 1992, ApJ, 392, L47
- Franx, M., Illingworth, G., & de Zeeuw, T. 1991, ApJ, 383, 112
- Franx, M., van Gorkom, J. H., & de Zeeuw, T. 1994, ApJ, 436, 642
- Frenk, C. S., White, S. D. M., Davis, M., & Efstathiou, G. 1988, ApJ, 327, 507
- Fridman, T., & Merritt, D. 1997, AJ, 114, 1479
- Gerhard, O. E., & Binney, J. 1985, MNRAS, 216, 467
- Gerhard, O. E., & Vietri, M. 1986, MNRAS, 223, 377
- Ghigna, S., Moore, B., Governato, F., Lake, G., Quinn, T., & Stadel, J. 2000, ApJ, 544, 616
- Governato, F., et al. 2004, ApJ, 607, 688
- Governato, F., Willman, B., Mayer, L., Brooks, A., Stinson, G., Valenzuela, O., Wadsley, J., & Quinn, T. 2007, MNRAS, 374, 1479
- Helmi, A. 2004, MNRAS, 351, 643
- Holley-Bockelmann, K., Mihos, J. C., Sigurdsson, S., Hernquist, L., & Norman, C. 2002, ApJ, 567, 817
- Huizinga, J. E., & van Albada, T. S. 1992, MNRAS, 254, 677
- Ibata, R., Lewis, G. F., Irwin, M., Totten, E., & Quinn, T. 2001, ApJ, 551, 294
- Ideta, M., & Hozumi, S. 2000, ApJ, 535, L91
- Iodice, E., Arnaboldi, M., Bournaud, F., Combes, F., Sparke, L. S., van Driel, W., & Capaccioli, M. 2003, ApJ, 585, 730
- Jimenez, R., Verde, L., & Oh, S. P. 2003, MNRAS, 339, 243
- Jing, Y. P., & Suto, Y. 2002, ApJ, 574, 538
- Johnston, K. V., Law, D. R., & Majewski, S. R. 2005, ApJ, 619, 800

- Jungman, G., Kamionkowski, M., & Griest, K. 1996, *Phys. Rep.*, 267, 195
- Kalapotharakos, C., Voglis, N., & Contopoulos, G. 2004, *A&A*, 428, 905
- Katz, N. 1991, *ApJ*, 368, 325
- Kazantzidis, S., Kravtsov, A. V., Zentner, A. R., Allgood, B., Nagai, D., & Moore, B. 2004, *ApJ*, 611, L73
- Kazantzidis, S., Magorrian, J., & Moore, B. 2004, *ApJ*, 601, 37
- Klypin, A., Gottlöber, S., Kravtsov, A. V., & Khokhlov, A. M. 1999, *ApJ*, 516, 530
- Kochanek, C. S. 1995, *ApJ*, 445, 559
- Koopmans, L. V. E., de Bruyn, A. G., & Jackson, N. 1998, *MNRAS*, 295, 534
- Kuijken, K., & Tremaine, S. 1994, *ApJ*, 421, 178
- Lake, G., & Norman, C. 1983, *ApJ*, 270, 51
- Macciò, A. V., Sideris, I., Miranda, M., Moore, B., & Jesseit, R. 2007, *ArXiv e-prints*, 704
- Mashchenko, S., Couchman, H. M. P., & Wadsley, J. 2006, *Nature*, 442, 539
- Mayer, L., Kazantzidis, S., Mastropietro, C., & Wadsley, J. 2007, *Nature*, 445, 738
- Merritt, D., & Poon, M. Y. 2004, *ApJ*, 606, 788
- Merritt, D., & Quinlan, G. D. 1998, *ApJ*, 498, 625
- Moore, B., Ghigna, S., Governato, F., Lake, G., Quinn, T., Stadel, J., & Tozzi, P. 1999, *ApJ*, 524, L19
- Moore, B., Kazantzidis, S., Diemand, J., & Stadel, J. 2004, *MNRAS*, 354, 522
- Navarro, J. F., & Steinmetz, M. 1997, *ApJ*, 478, 13
- Norman, C. A., May, A., & van Albada, T. S. 1985, *ApJ*, 296, 20
- Oguri, M., Lee, J., & Suto, Y. 2003, *ApJ*, 599, 7
- Poon, M. Y., & Merritt, D. 2002, *ApJ*, 568, L89
- Porciani, C., Dekel, A., & Hoffman, Y. 2002, *MNRAS*, 332, 325

- Read, J. I., Goerdt, T., Moore, B., Pontzen, A. P., Stadel, J., & Lake, G. 2006, MNRAS, 373, 1451
- Sackett, P. D., & Sparke, L. S. 1990, ApJ, 361, 408
- Schoenmakers, R. H. M., Franx, M., & de Zeeuw, P. T. 1997, MNRAS, 292, 349
- Schwarzschild, M. 1979, ApJ, 232, 236
- Schweizer, F., Whitmore, B. C., & Rubin, V. C. 1983, AJ, 88, 909
- Shen, J., & Sellwood, J. A. 2004, ApJ, 604, 614
- Sommer-Larsen, J., Gelato, S., & Vedel, H. 1999, ApJ, 519, 501
- Spergel, D. N., & et al. 2006, astro-ph/0603449
- Stadel, J. G. 2001, Ph.D. Thesis, University of Washington
- Statler, T. S. 1987, ApJ, 321, 113
- Tonini, C., Lapi, A., & Salucci, P. 2006, ApJ, 649, 591
- Udry, S., & Martinet, L. 1994, A&A, 281, 314
- Valluri, M., & Merritt, D. 1998, ApJ, 506, 686
- van den Bosch, F. C., Abel, T., Croft, R. A. C., Hernquist, L., & White, S. D. M. 2002, ApJ, 576, 21
- Warren, M. S., Quinn, P. J., Salmon, J. K., & Zurek, W. H. 1992, ApJ, 399, 405
- Weijmans, A.-M., Krajnovic, D., van de Ven, G., Oosterloo, T. A., Morganti, R., & de Zeeuw, P. T. 2007, ArXiv e-prints, 711
- Weinberg, M. D. 1985, MNRAS, 213, 451
- Weinberg, M. D., & Katz, N. 2007, MNRAS, 375, 425
- Zentner, A. R., Kravtsov, A. V., Gnedin, O. Y., & Klypin, A. A. 2005, ApJ, 629, 219

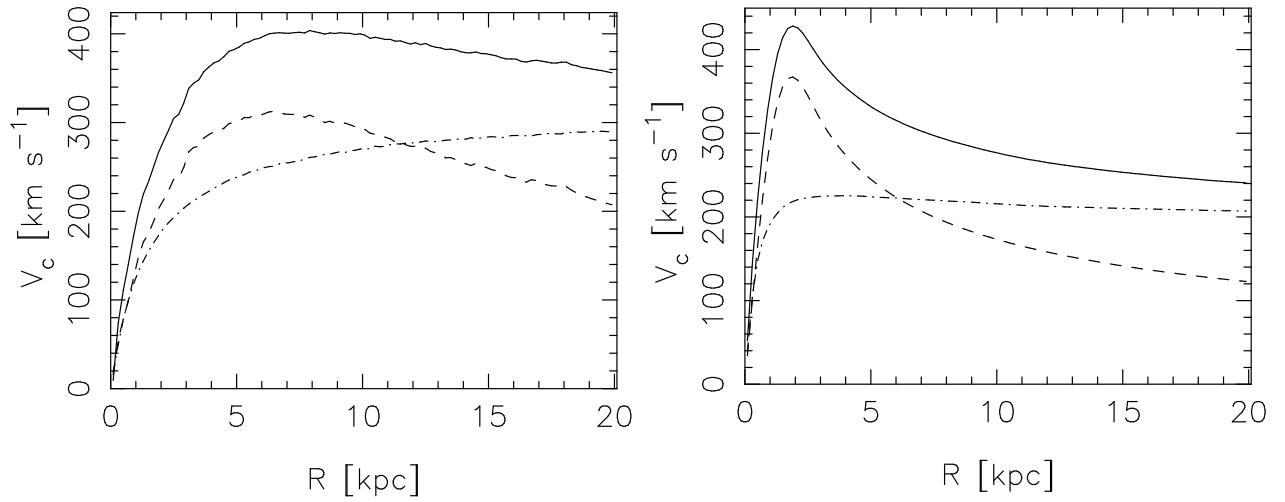


Fig. 2.— Azimuthally averaged rotation curves of models SA1 (*left*) and P_lB1/P_fB2 (*right*) measured in the midplane. In both panels the solid line is the full rotation curve, the dashed line the contribution of the baryons, and the dot-dashed line the contribution from the halo.

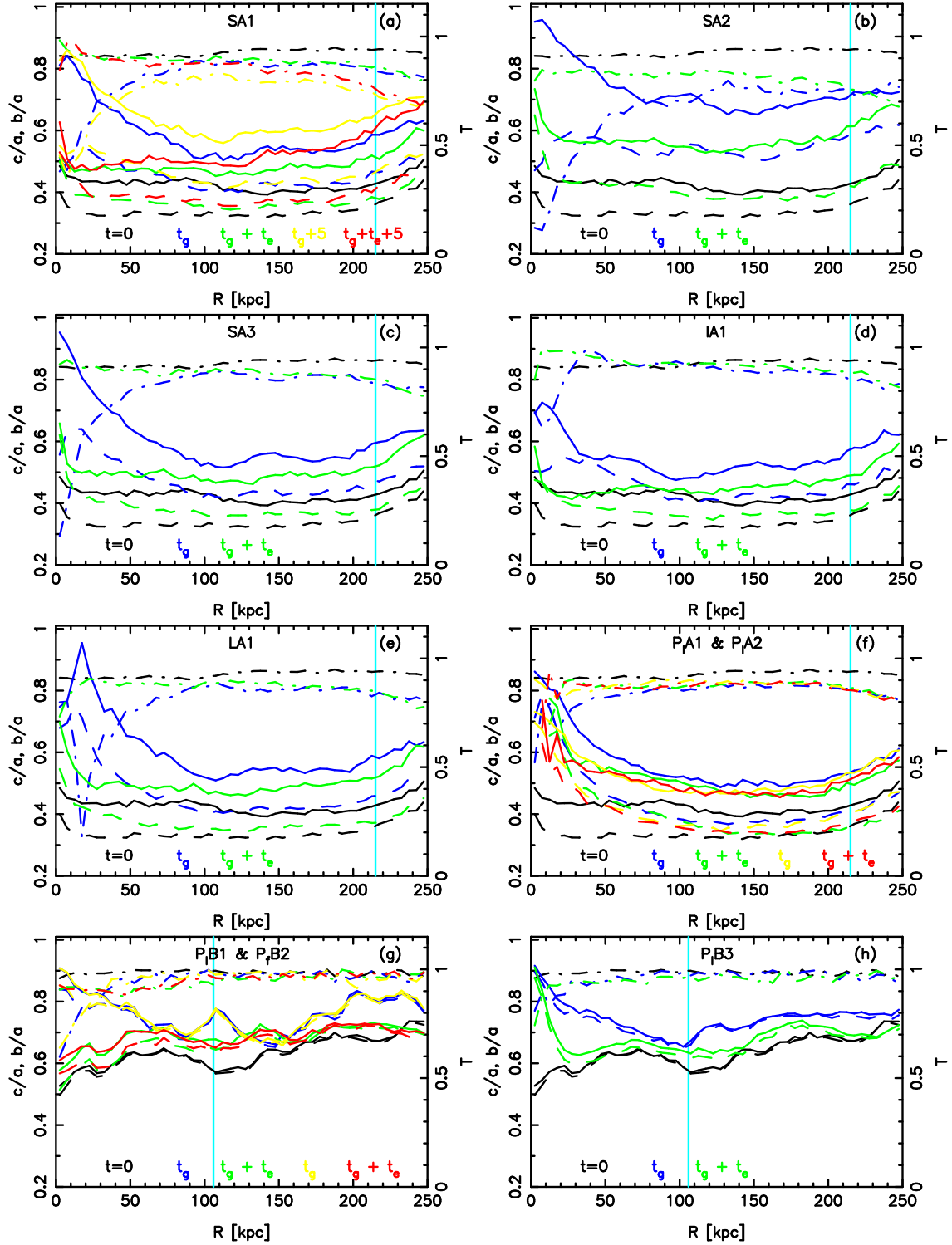


Fig. 3.— Shape evolution in runs (a) SA1, (b) SA2, (c) SA3, (d) IA1, (e) LA1, (f) P_lA1 and P_lA2, (g) P_lB1 and P_fB2 and (h) P_lB3. The solid lines show b/a , the dashed lines show c/a , and the dot-dashed lines show T (with scale indicated on the right-hand side of each panel). The black, blue, and green lines are at $t = 0$, t_g , and $t_g + t_e$, respectively. In panel (a) black/yellow/red shows the evolution if, after t_g , the disk is held at full mass for a further 5 Gyr before it is evaporated. In panel (f), the standard colors are for P_lA1, while P_lA2 is indicated in black/yellow/red. Likewise, in panel (g), the standard colors are for P_fB2,

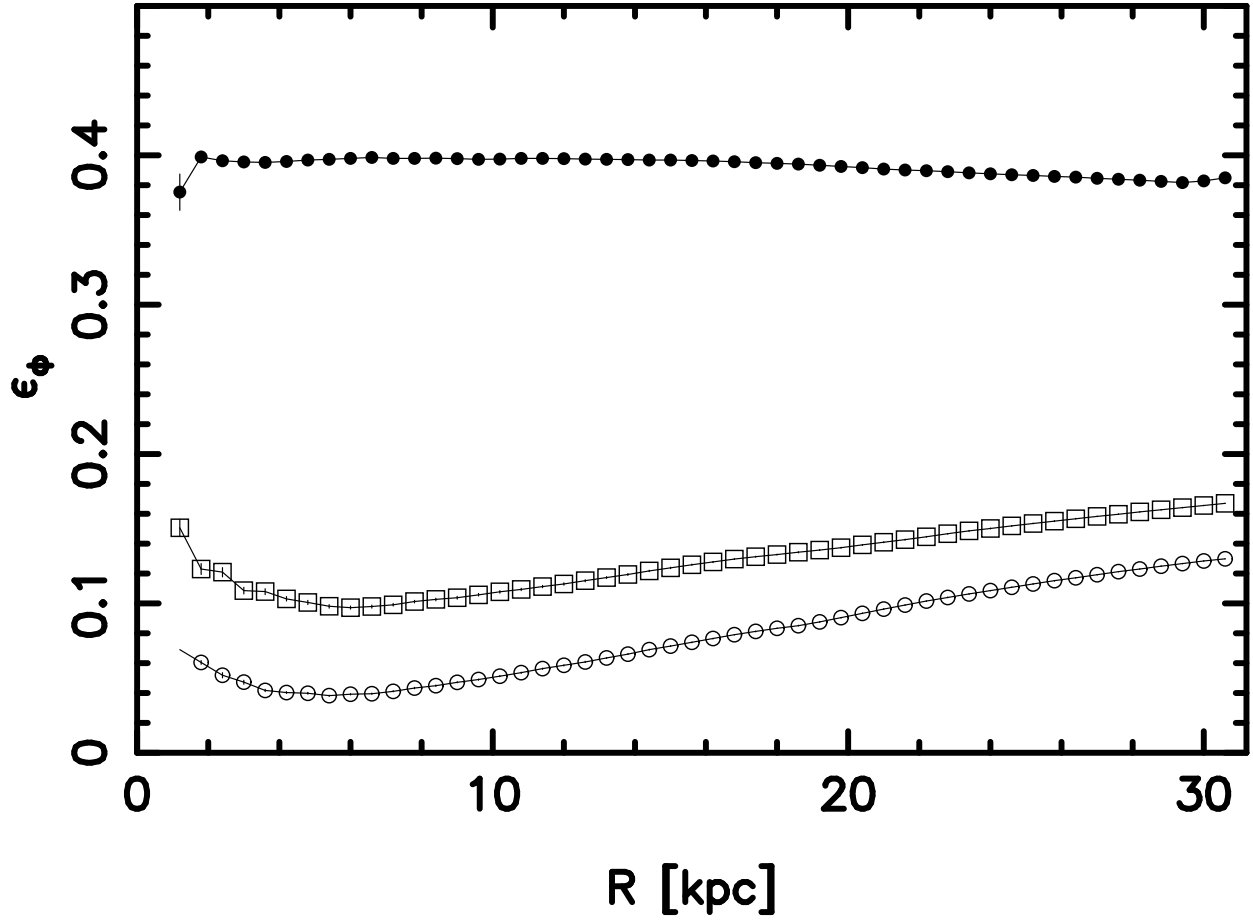


Fig. 4.— Ellipticity of the potential, ϵ_ϕ , in the disk mid-plane of run SA1. The solid points are at $t = 0$, and the open points are at t_g , with squares for halo only and circles for disk+halo.

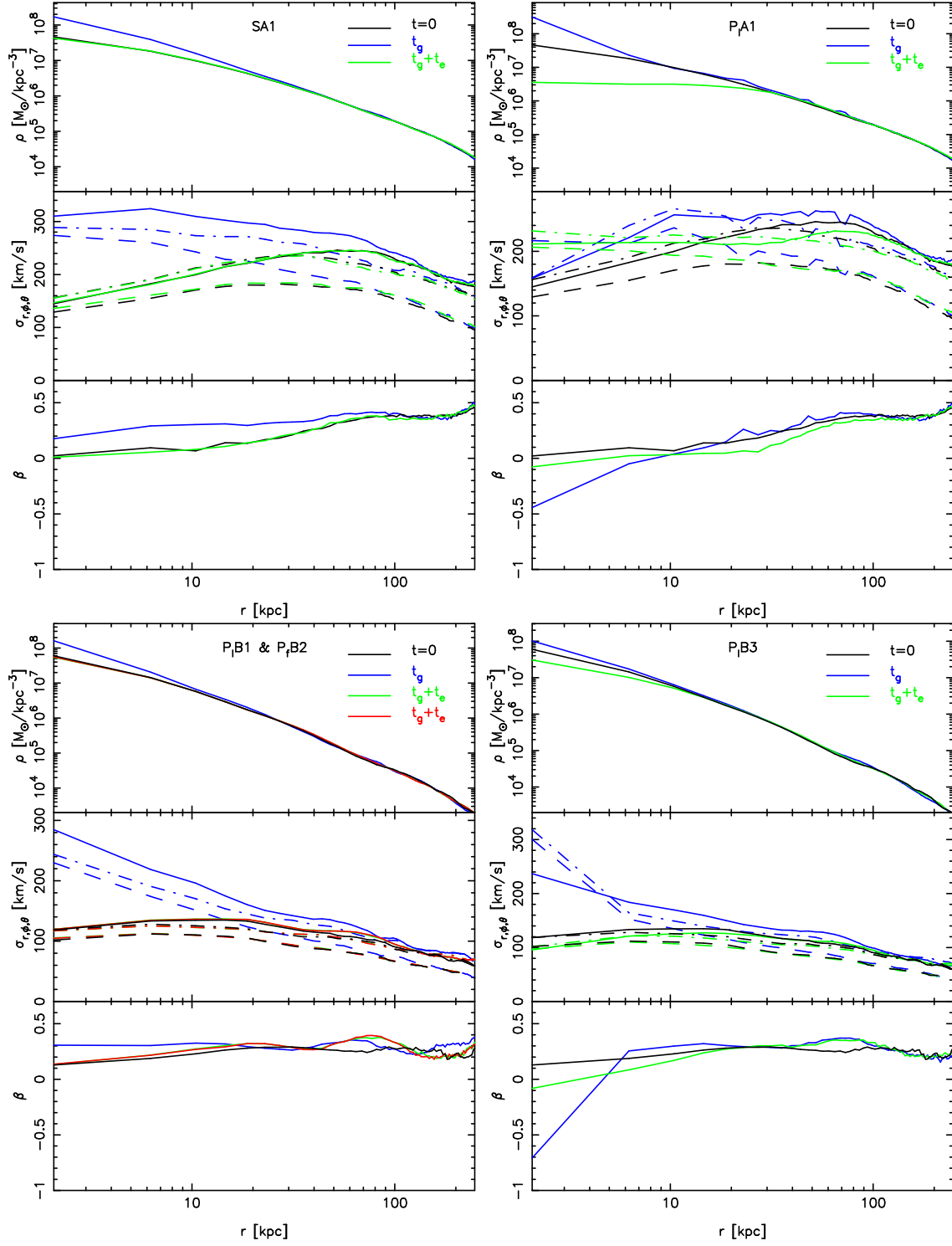


Fig. 5.— Evolution of the spherically averaged density and kinematics in runs SA1 (*top left*), P_lA1 (*top right*), P_lB1 and P_fB2 (*bottom left*), and P_lB3 (*bottom right*). The black, blue, and green lines correspond to $t = 0$, t_g , and $t_g + t_e$. The red lines show $t_g + t_e$ for P_fB2 . The top panels shows the densities. In the middle panels the solid lines indicate σ_r , the dashed lines σ_ϕ , and the dot-dashed lines σ_θ . Here the z -axis from which the angle θ is measured is the long axis of the halo. The bottom panels show the anisotropy parameter, β .

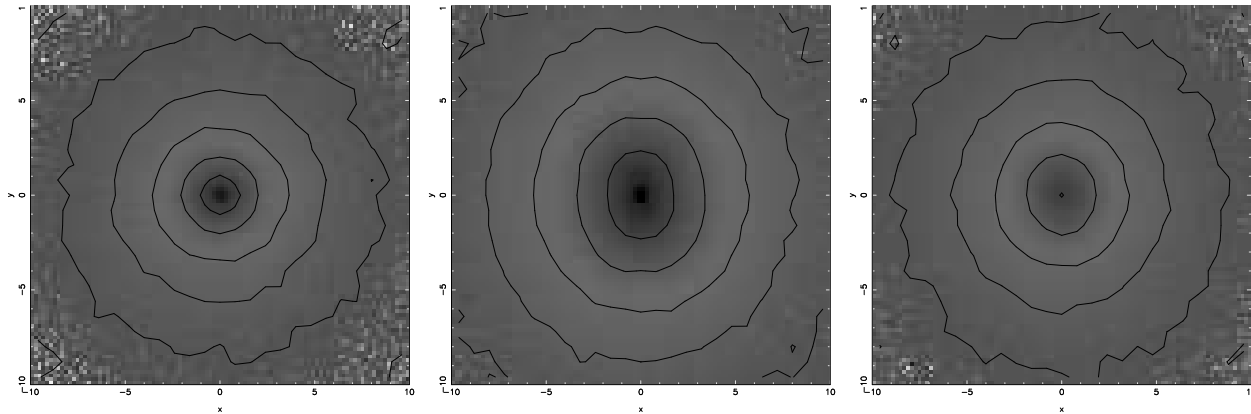


Fig. 6.— Evolution of the inner halo in run LB1, seen in cross section in the disk plane, with only the region $|z| < 5$ kpc shown, where the z -axis is the symmetry axis of both disk and halo. The panels show $t = 0$ (*left*), t_g (*middle*) and $t_g + t_e$ (*right*). The halo is initially axisymmetric, becomes elongated orthogonal to the symmetry axis at small radii at t_g , and largely recovers its axisymmetry at $t_g + t_e$.

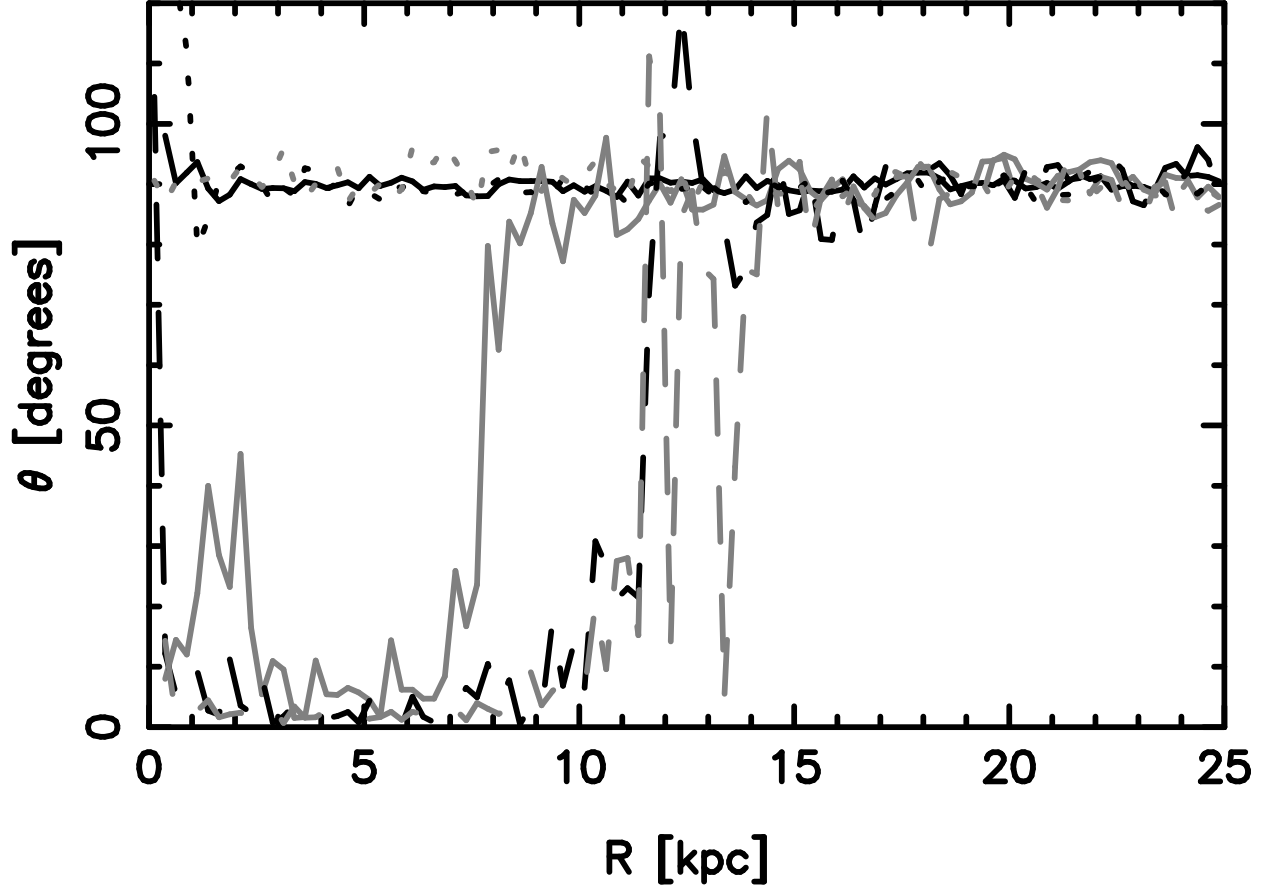


Fig. 7.— Major axis orientation evolution in run LB1. The solid black and gray lines are at $t = 0$ and $t_g/3$, the dashed black and gray lines are at $2t_g/3$ and t_g and the black dotted line is at $t_g + t_e$. The gray dotted line shows run P_lB1 at t_g .

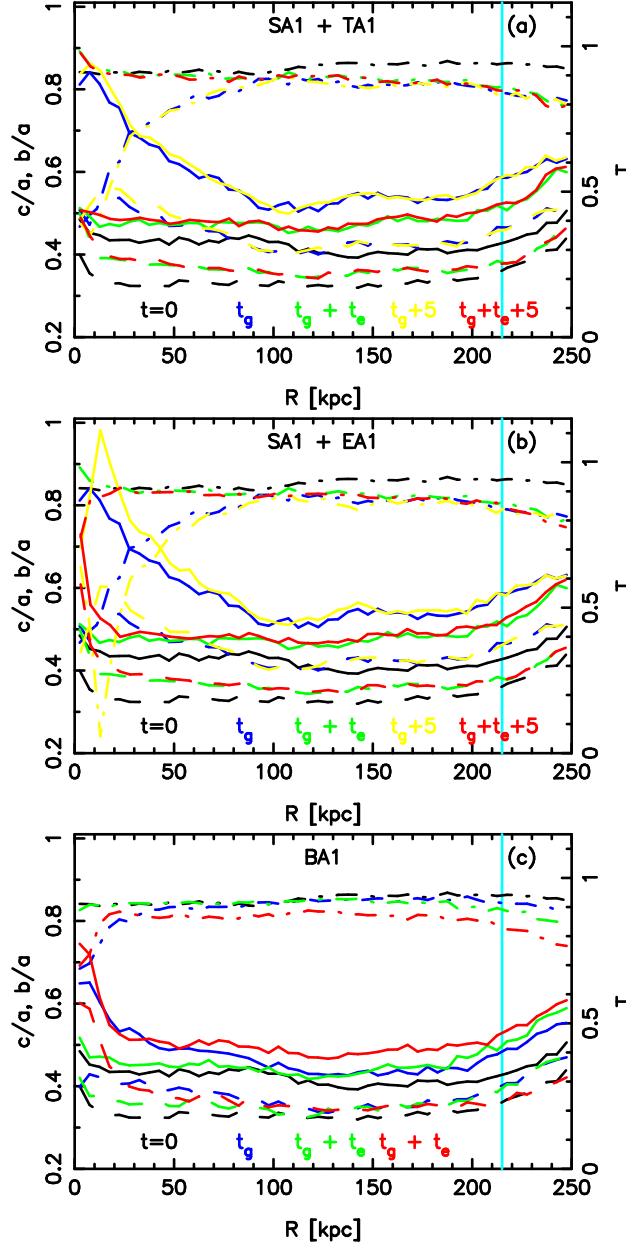


Fig. 8.— Shape evolution in runs (a) TA1, (b) EA1, and (c) BA1. The solid lines show b/a , the dashed lines show c/a and the dot-dashed lines show T (with scale indicated on the right hand side of each panel). The black, yellow, and red lines show $t = 0$, t_g , and $t_g + t_e$. For comparison, the equivalent evolution for run SA1 is shown by the blue and green lines.

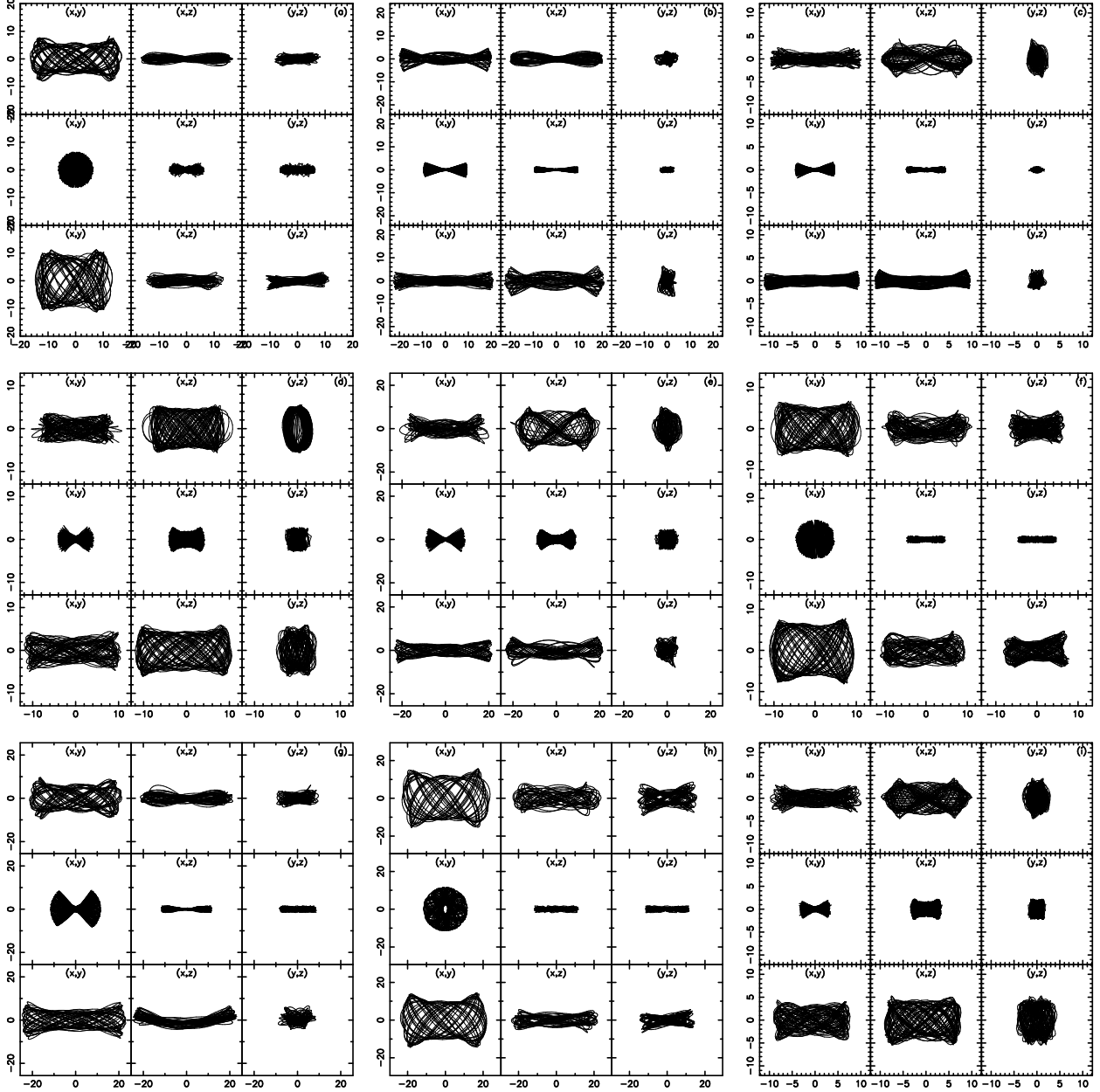


Fig. 9.— Sample of initially boxlike orbits in run SA1. In each set of panels, the top row is at $t = 0$, the middle row is at t_g , and the bottom row is at $t_g + t_e$; from left to right the panels show projections onto the (x, y) , (x, z) , and (y, z) planes. Each orbit has been integrated for 15 Gyr from each of $t = 0$, t_g and $t_g + t_e$.

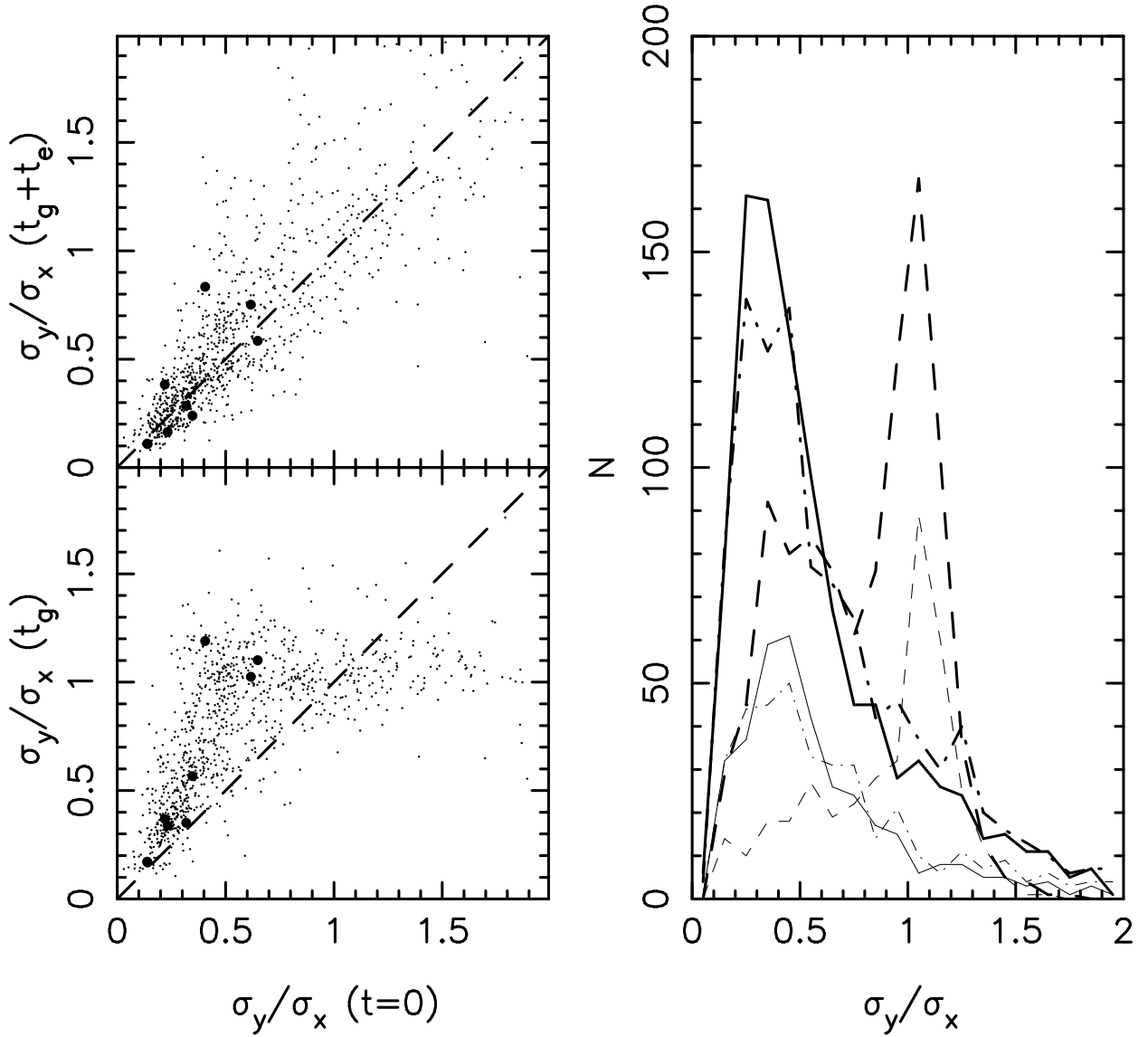


Fig. 10.— Deformation of orbits in run SA1. In the left panels, the dashed line shows the diagonal. The solid points show the nine particles of Fig. 9. In the right panel, the solid, dashed, and dot-dashed lines show the distributions at $t = 0$, t_g , and $t_g + t_e$, respectively. The thick lines are for the full distribution of 1000 particles, while the thin lines are for those particles that remain inside $r = 50$ kpc during the 15 Gyr integration starting at $t = 0$.

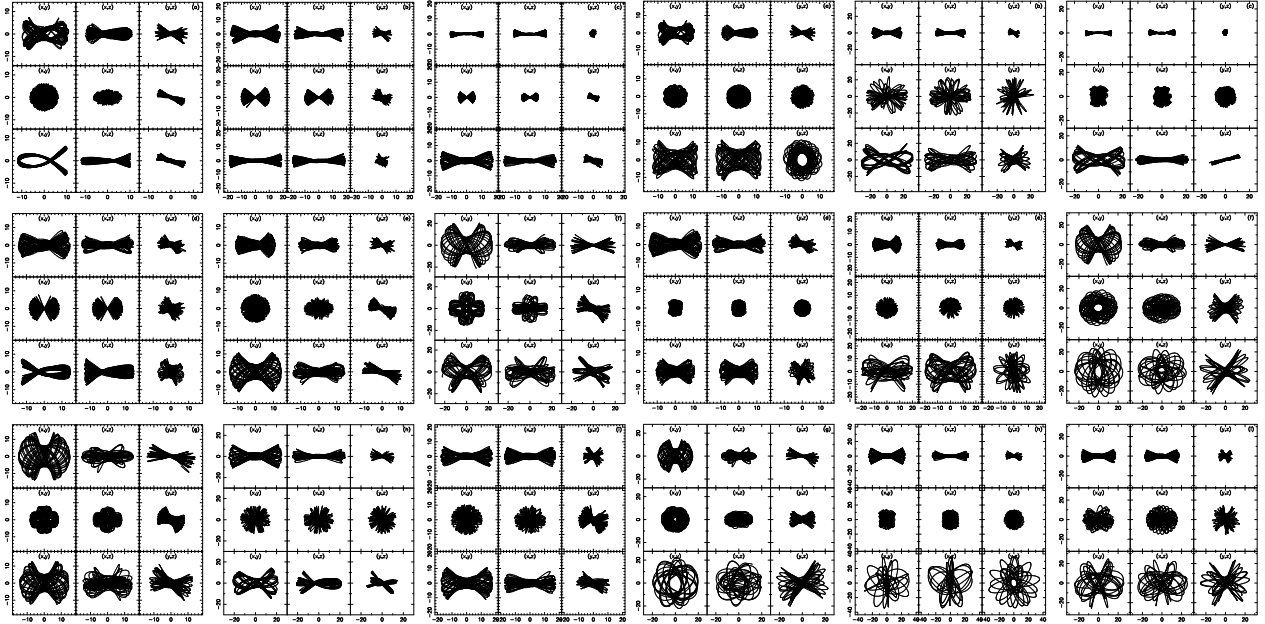


Fig. 11.— Sample of initially boxlike orbits in run P_fB2 (left three columns) and P_lB3 (right three columns). We show the evolution of the same nine starting orbits in the two different models. In each set of panels, the top row is at $t = 0$, the middle row is at $t_g/2$ (P_fB2) or t_g (P_lB3), and the bottom row is at $t_g + t_e$; from left to right the panels show projections onto the (x, y) , (x, z) , and (y, z) planes. Each orbit has been integrated for 15 Gyr from each starting point.

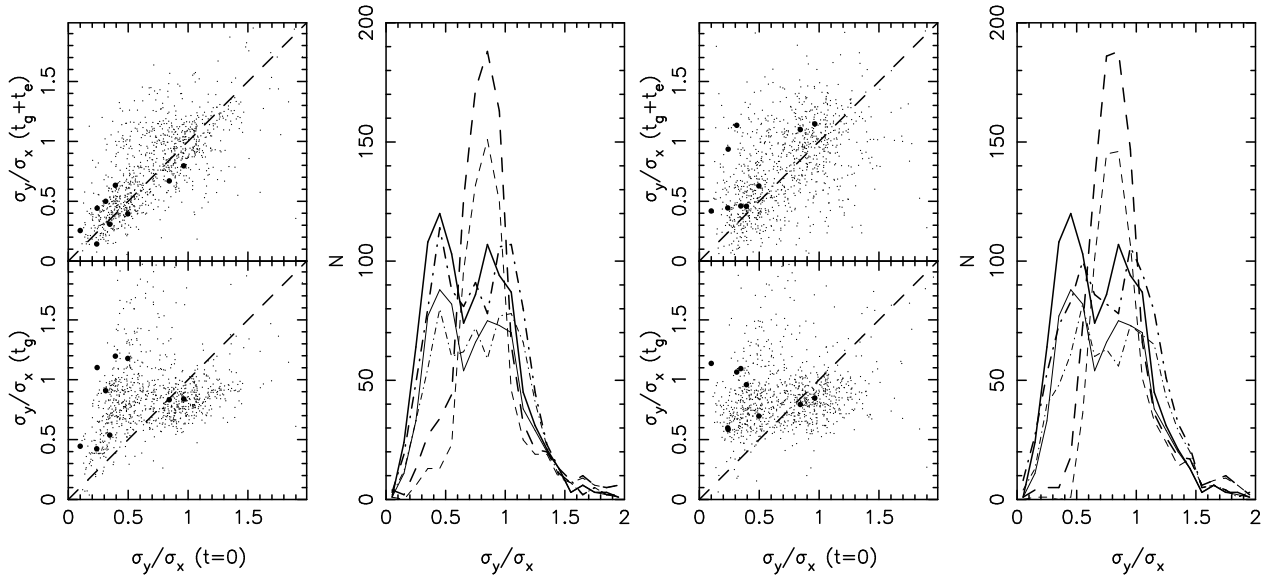


Fig. 12.— Identical to Fig. 10 but for runs P_fB2 (*left*) and P_lB3 (*right*). The final distribution of orbits is significantly depleted of elongated orbits in run P_lB3 compared with run P_fB2 . All nine orbits of Fig. 11 are above the diagonal in run P_lB3 at $t_g + t_e$ but scatter about the diagonal in run P_fB2 .

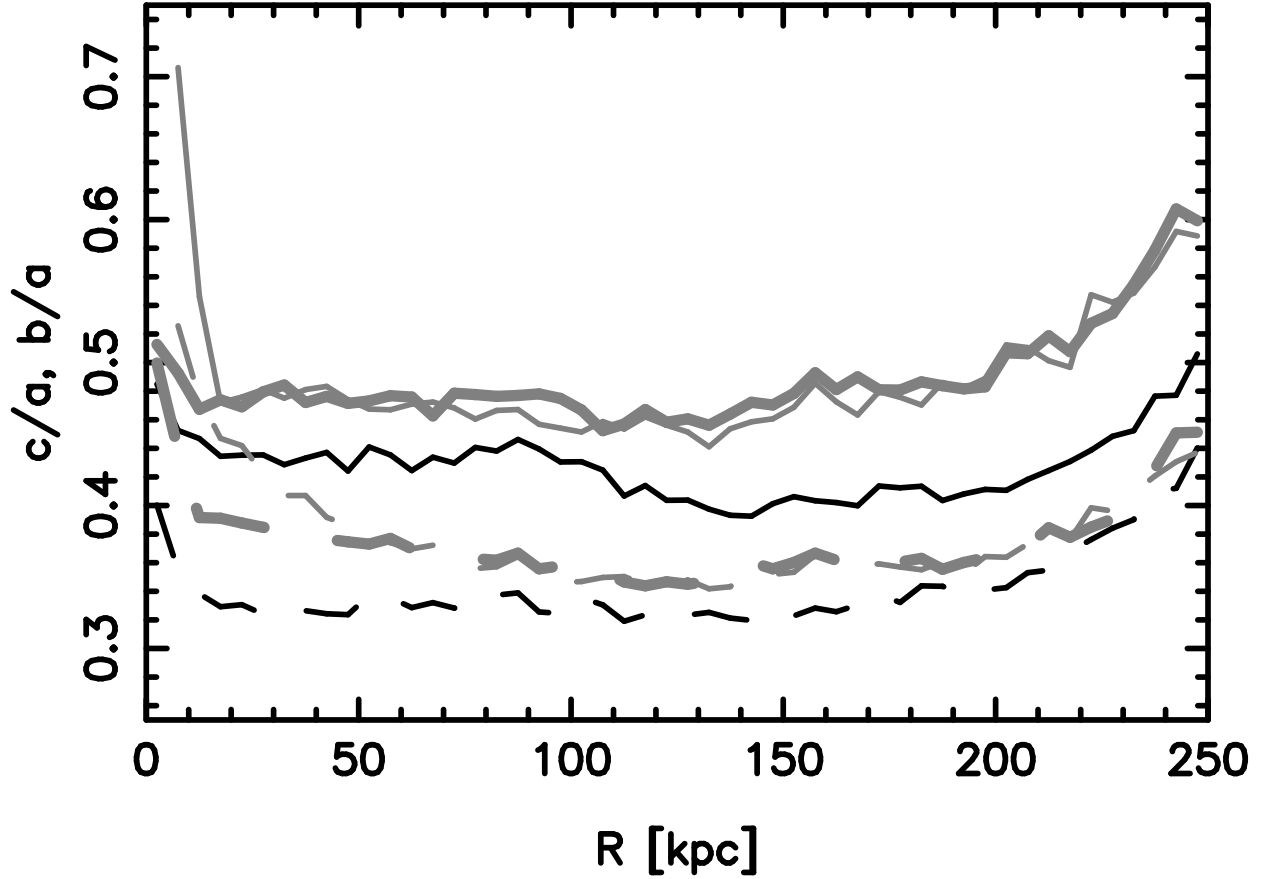


Fig. 13.— Effect of timestep size on the evolution of run SA1. The black lines shows the shape at $t = 0$ while the gray lines are for $t_g + t_e$, with the thick line the standard result with $\eta = 0.2$ and the thin lines for $\eta = 2$. As in Fig. 3, the solid lines show b/a while the dashed lines show c/a . The larger timesteps lead to an evolution that is less reversible.